Journal of Materials Chemistry A

Accepted Manuscript

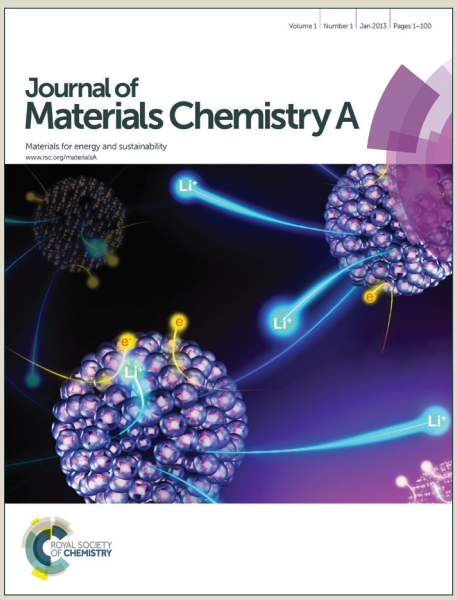

ROYAL SOCIETY OF CHEMISTRY

www.rsc.org/materialsA

Cite this: DOI: 10.1039/c0xx00000x

www.rsc.org/xxxxxx

ARTICLE TYPE

Preparing $LiNi_{0.5}Mn_{1.5}O_4$ Nanoplates with Superior Properties in Lithium-ion Batteries Using Bimetal-Organic Coordination-Polymer as Precursors

Shifeng Yang,[a,b] Jian Chen,[*a] Yingjia Liu[a] and Baolian Yi[a]

Received (in XXX, XXX) Xth XXXXXXXXX 20XX, Accepted Xth XXXXXXXXX 20XX
DOI: 10.1039/b000000x

$LiNi_{0.5}Mn_{1.5}O_4$ nanoplates were prepared using a two-step method composed of hydrothermal method and solid-state reaction. At first, the bimetal-organic coordination-polymers containing Ni^{2+} and Mn^{2+} were synthesized using the ligand of 3,4,9,10-perylenetetracarboxylic dianhydride (ptcda) by a template-assisted self-assembly method in the hydrothermal atmosphere. Followed by the thermal treatment to remove the organic components and then calcination with lithium acetate, the nanoplate-stacked $LiNi_{0.5}Mn_{1.5}O_4$ was obtained. The nanoplate structure shortens the diffusion path of lithium ions in the bulk of $LiNi_{0.5}Mn_{1.5}O_4$ and then promotes the fast charge-discharge property of the material. Besides, an amorphous Li_2CO_3 layer with nanometer thickness in-situ generated on the surface of $LiNi_{0.5}Mn_{1.5}O_4$ particles is confirmed by TEM and XPS. It is helpful for suppressing the interfacial side reactions and thereby improving the cycling stability of the materials. Owing to these advantages, the $LiNi_{0.5}Mn_{1.5}O_4/Li_2CO_3$ materials exhibit excellent rate capability and cycling stability. The as-prepared material delivers 129.8 mAh g^{-1} at 1 C rate and retains 86.4% of the initial capacity even after 1000 cycles of charge-discharge at 25 °C. Even at a high discharge rate of 40 C, the specific capacity of the materials is 120.9 mAh g^{-1}, and the capacity retention is 84.7% over 500 cycles. The high-temperature stability of the material is also superior. When operating at 55 °C, the capacity loss by cycle is only 0.037% throughout 250 cycles.

1 Introduction

Developing the new generation of lithium-ion battery (LIB) with high density of energy and power is urgently required to meet the increasing demand of the emerging applications in plug-in hybrid-electric vehicles (PHEVs) and electric vehicles (EVs). This in turn, depends critically on the research and development of novel cathode materials. The spinel $LiNi_{0.5}Mn_{1.5}O_4$ with a stable discharge potential plateau as high as ~ 4.7 V (vs. Li/Li^+) and theoretical specific capacity of 147 mAh g^{-1}, as well as good rate capability benefiting from the three dimensional channels for Li^+ transfer, could make LIBs with promising high density of energy and power.

$LiNi_{0.5}Mn_{1.5}O_4$ has two different crystal structures of simple cubic structure ($P4_332$) and face-centered cubic structure ($Fd\bar{3}m$).[1-3] The $P4_332$ typed $LiNi_{0.5}Mn_{1.5}O_4$ is stoichoimetric, and the valence of Mn in the molecule is +4. The $Fd\bar{3}m$ one is the nonstoichoimetric $LiNi_{0.5}Mn_{1.5}O_{4-\triangle}$ containing a trace of Mn^{3+} [4, 5] which is generated from the oxygen loss from the crystal lattice during sintering at high temperatures (> 800 °C) and insufficient oxygen uptake during cooling.[4, 6, 7] Owing to the fast electron hopping between Ni^{2+} and Mn^{3+}, the $Fd\bar{3}m$ structured $LiNi_{0.5}Mn_{1.5}O_4$ has 1.5 ~ 2.5 orders of magnitude higher electronic conductivity than the $P4_332$ one.[3, 8]

Despite these advantages, the $Fd\bar{3}m$ structured $LiNi_{0.5}Mn_{1.5}O_4$ easily suffers from capacity fading, which will be more severe at elevated operating temperature such as 50 ~ 60 °C. The capacity fading issue is mainly caused by two factors: decomposition of the electrolyte and dissolution of the transition metal ions. When operating at a high potential, such as 5 V (vs. Li/Li^+), the products of electrolyte decomposition will react with the active materials of $LiNi_{0.5}Mn_{1.5}O_4$.[9-11] As a result, a large amount of Ni and Mn will dissolve in the solution, which is the main reason for the capacity loss of the material.[9, 10] Moreover, both the decomposition of electrolyte and dissolution of the transition metal ions can be accelerated at elevated temperature, which will further deteriorate the capacity retention of the material.[9-11] While unlike $LiMn_2O_4$, the nonstoichoimetric $LiNi_{0.5}Mn_{1.5}O_{4-\triangle}$ contains much smaller portion of Mn(□), in addition, the discharge cut-off voltage of the material is above 3.2 V, and thus the Jahn–Teller effect and the dissolution and loss of Mn^{2+} via the disproportionation caused by Mn^{3+} become less serious.[12] Coupled to the capacity fading, oxygen releases from the crystal lattice during the process of high temperature synthesis, thereby causing the distortion of the Mn, Ni(12d)-O octahedral site[13] that often leads to the formation of rock-salt $Li_xNi_{1-x}O$ impurity ($LiNi_{0.5}Mn_{1.5}O_4 \rightarrow Li_xNi_{1-x}O + LiMn_{1.5+y}Ni_{0.5-y}O_{4-z} + O_2$ at T>700 °C).[6, 7, 14] The common concomitant $Li_xNi_{1-x}O$ phase existing in the $LiNi_{0.5}Mn_{1.5}O_4$ materials will result in the low accessible capacity and structural instability.[6, 14, 15]

In recent years, three kinds of strategy have been developed to improve the electrochemical performance of $LiNi_{0.5}Mn_{1.5}O_4$ cathode material: lattice doping, surface coating and novel synthesis method. It has been proved that lattice doping including metal cation substitution with Al, Cu, Zn, Fe, Mg Ti, Co, Ru, Cr[16-24] and anion doping like F^-[22] is quite effective to eliminate the formation of $Li_xNi_{1-x}O$ and stabilize the spinel structure of

$LiNi_{0.5}Mn_{1.5}O_4$, thus improving the capacity and cycling performance of the material. For example, when charging-discharging at 1 C rate, the capacity retention for $LiCr_{0.2}Ni_{0.4}Mn_{1.4}O_4$ after 250 cycles at 55 °C was 97.3%,[25] and for $LiNi_{0.45}Co_{0.10}Mn_{1.45}O_4$ after 500 cycles at room temperature was nearly 96.0%.[23] Metal oxides, such as ZnO, Al_2O_3, Bi_2O_3, $La_{0.7}Sr_{0.3}MnO_3$, $LiFePO_4$, $Li_4P_2O_7$ and $LiCoO_2/Co_3O_4$ [20, 26-29] have been employed to improve the cycling stability as a protective surface layer by suppressing the dissolution of Mn into the electrolyte. It has been reported that the $Li_4P_2O_7$-stabilized $LiNi_{0.5}Mn_{1.5}O_4$ delivered a specific capacity of 123.8 mAh g^{-1} and retained 74.3% of the initial capacity after 893 cycles at 0.5 C.[29] Novel synthesis methods can surprisingly improve the electrochemical performance. $LiNi_{0.5}Mn_{1.5}O_4$ cathode material prepared using a urea-based sol–gel method delivered a specific discharge capacity of 97.8 mAh g^{-1} and remained 87.5% of the initial capacity after 200 cycles at 20 C rate.[30] The $LiNi_{0.5}Mn_{1.5}O_4$ with a hierarchical porous structure prepared using a cotton-template method remained more than 92% of the initial capacity after 400 cycles of charging-discharging at 5 C rate.[31] The similar cycling stability at high discharge rates was also exhibited by $LiNi_{0.5}Mn_{1.5}O_4$ porous nanorods prepared from 1D porous Mn_2O_3.[32] Although much progress has been made so far, the cycling stability and rate capability of the $LiNi_{0.5}Mn_{1.5}O_4$ are still unsatisfactory for its application in PHEVs and EVs.

Since the electrochemical performance of the cathode materials for Li-ion batteries is to some extent determined by the diffusion of Li^+ in the bulk of the material, it can be greatly improved by reducing the particle size of the material to nano-size. 3,4,9,10-perylenetetracarboxylic dianhydride (ptcda), a kind of ligand, has a rigid and planar molecular structure which guides its derivatives to inherit the similar lamellar structure.[33-35] Spinel mixed-metal oxides MMn_2O_4 (M=Co, Ni, Zn) nanoplate assemblies have been successfully synthesized using the ptcda by Zhao and her co-workers.[35] It can be expected to synthesize $LiNi_{0.5}Mn_{1.5}O_4$ nanoplates with the assistance of ptcda using the mixed metal-organic coordination-polymer as the precursor. In addition, it has been confirmed that the SEI layer mainly composed of Li_2CO_3 can effectively protect the carbon anode from the reactions between the anode and electrolyte.[36] The Li_2CO_3-coated lithium metal electrode also exhibits better cycling stability than the raw one.[37] Herein, the in-situ generation of amorphous Li_2CO_3 layer was conducted on the surface of nanoplate-structured $LiNi_{0.5}Mn_{1.5}O_4$ particles. The designed $LiNi_{0.5}Mn_{1.5}O_4$ nanoplate materials with a nano-scale Li_2CO_3 surface layer are expected to possess excellent cycling performance and rate capability.

2 Experimental Methods

2.1 Material Preparation

2.1.1 Synthesis of metal-organic coordination-polymers (CPs)

In a typical synthesis route,[35] $Mn(CH_3COO)_2{\cdot}4H_2O$ (0.7 mmol, □99.0%) and $Ni(CH_3COO)_2{\cdot}4H_2O$ (0.2 mmol, □98.0%) were dissolved in 25 mL de-ionized water, while 0.45 mmol ptcda (Alfa, 98.0%) was dissolved in 14 mL 0.128 M NaOH solution. The ptcda solution was added dropwise to the mixture solution of metal acetates. Afterwards, the mixed solution was under vigorous stirring for 0.5 h. The Ni, Mn-organic coordination-polymers (NiMn-CPs) were obtained by heating the mixture in a Teflon-lined stainless steel vessel at 100 °C for 24 h. After cooling down to room temperature, the precipitate was washed with the deionized water for 6 times to remove the residual sodium species, and then dried overnight.

2.1.2 Synthesis of $LiNi_{0.5}Mn_{1.5}O_4$ spinel cathode material from NiMn-CPs

Bimetal oxides of nickel and manganese (Ni-Mn-O) were obtained by thermal treating the NiMn-CPs at 550 °C for 1 h in flowing air. The obtained Ni-Mn-O were then grounded with excess 8%, 15% and 20% $LiCH_3COO{\cdot}2H_2O$, respectively, compared to the stoichiometric amount. The final product $LiNi_{0.5}Mn_{1.5}O_4$ was obtained by sintering the mixture at 850 °C for 12 h. Henceforth the samples of $LiNi_{0.5}Mn_{1.5}O_4$ are denoted as "+8%", "+15%" and "+20%", corresponding to the excess amount of lithium salts used.

2.2 Physical Characterization

The crystal structural and phase analyses of the prepared $LiNi_{0.5}Mn_{1.5}O_4$ materials were carried out by a X-ray diffractometer (Rigaku D/Max2500 PC) employing Cu K_a radiation with a scanning rate of 5°/min between 10° and 80°. The compositions of the materials were characterized by inductively coupled plasma spectrometry ICP (Optima 2000 DV).

The Raman spectrum was collected on Ray Nepal Shao significant micro confocal Raman spectrometer, using an excitation light of 514.5 nm from Ar ion laser. The morphology of the $LiNi_{0.5}Mn_{1.5}O_4$ particles was characterized using scanning electron microscopy (SEM, JSM-6360) and transmission electron microscopy (TEM, Hitachi HT7700 and FEI TECNAI G2 F30).

2.3 Electrochemical Performance Tests

2.3.1 Cell Assembly

The electrochemical performance of the $LiNi_{0.5}Mn_{1.5}O_4$ cathode material was evaluated with standard CR2016 coin cells. The cathode was fabricated by blending the as-prepared $LiNi_{0.5}Mn_{1.5}O_4$ powders, acetylene black and polyvinylidene fluoride (PVDF) with a weight ratio of 75:15:10 in a solvent of N-methyl-2-pyrrolidone (NMP). Then the obtained slurry was cast onto an aluminum foil and dried overnight at 58 °C in a vacuum. The lithium metal was used as the anode. CR2016 type coin cells were assembled in an argon-filled glove box with the electrolyte of 1.0 mol L^{-1} $LiPF_6$ dissolved in a mixture of ethylene carbonate (EC), dimethyl carbonate (DMC) and ethyl methyl carbonate (EMC) with 1:1:1 by weight.

2.3.2 Electrochemical Measurements

The charge-discharge tests were performed by galvanostatically charging and discharging the coin cells in the voltage range of 3.5 ~ 5.0 V on a Land battery test system (LANHE, CT2001A). The rate capability was assessed with the cell charged at 1 C and discharged at various rates from 1 C to 40 C, and then back to 1 C, where 1 C corresponds to 147 mA g^{-1}. The performance of the cycling stability of the materials at 25 °C and 55 °C was evaluated using a charge-discharge rate of 1 C. The cycling performance at discharge rates of 10 C and 40 C was also measured.

The cyclic voltammogram (CV) curve was measured using a coin cell on a CHI 605A electrochemical workstation (Shanghai Chen Hua Instrument Co., Ltd) in the potential range of 3.5 to 5.0

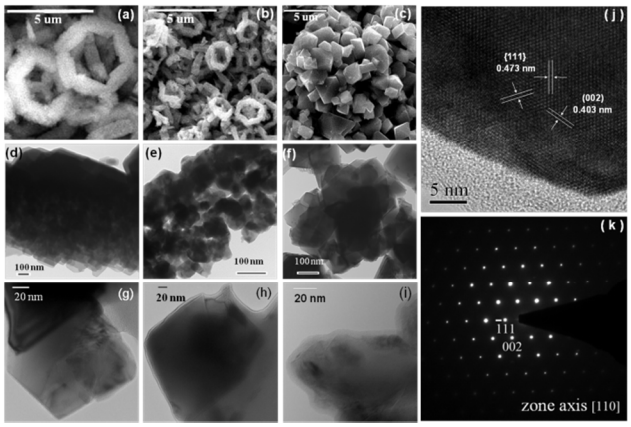

Fig. 1 SEM and TEM images. SEM images of (a) the NiMn-CPs precursors, (b) the Ni-Mn-O intermediates, and (c) the final product of $LiNi_{0.5}Mn_{1.5}O_4$ for the "+15%" sample; TEM images (d-f) corresponding to the particles in a-c, respectively; TEM images of the (g) +8%, (h) +15% and (i) +20% samples at a high magnification; (j) HRTEM images of the "+15%" $LiNi_{0.5}Mn_{1.5}O_4$ sample and (k) the corresponding SAED pattern.

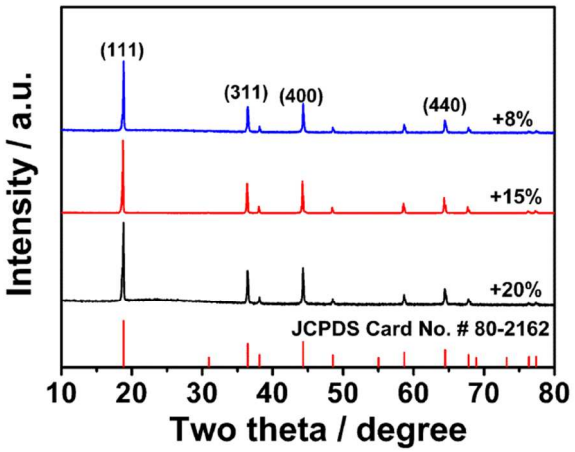

Fig. 2 X-ray diffraction patterns of the $LiNi_{0.5}Mn_{1.5}O_4$ samples prepared with excess 8%, 15% and 20% lithium salts.

V at a scan rate of 0.05 mV s^{-1}. The electrochemical impedance spectroscopy (EIS) analyses were carried out with AC amplitude of 5 mV in the frequency range of 1MHz to 10 mHz using the coin cell. In such cases, the $LiNi_{0.5}Mn_{1.5}O_4$ electrode was used as the working electrode, and the lithium electrode was employed as both the counter and reference electrode. The measurements were performed at room temperature.

3 Result and discussion

The morphologies of NiMn-CPs precursor, bimetal oxide Ni-Mn-O intermediate and the final product $LiNi_{0.5}Mn_{1.5}O_4$ were investigated using SEM and TEM, respectively, as shown in Fig. 1. After hydrothermal treatment of the mixed solution containing ptcda and transition metal ions of Ni^{2+} and Mn^{2+}, the obtained NiMn-CPs precursor has been confirmed by X-ray diffraction pattern (Fig. †S1) and IR spectroscopy (Fig. †S2). As shown in Fig. 1a, NiMn-CPs precursors are composed of hexagonal rings with the outer and inner dimensions of 4.8 and 2.8 μm and a thickness of 0.7 μm. The TEM image in Fig. 1d reveals that the hexagonal ring is assembled of nanoplates with uniform size. After thermal treatment at 550 °C , the organic components were removed to obtain the bimetal oxide Ni-Mn-O with a cubic spinel structure of the $Fd\bar{3}m$ space group, which has been confirmed by XRD characterization (shown in Fig.†S3). It can be observed from Fig. 1b that the Ni-Mn-O still remained the morphology of hexagonal rings. Then the final product was synthesized by calcinating the Ni-Mn-O intermediates with $LiCH_3COO{\cdot}2H_2O$ at 850 °C for 10 h. It is confirmed that the cubic $LiNi_{0.5}Mn_{1.5}O_4$ spinel has been synthesized (as shown in Fig. 2). The details will be discussed in the section of XRD characterizations. The SEM image of the as-prepared $LiNi_{0.5}Mn_{1.5}O_4$ is presented in Fig. 1c. It can be observed that the unique hexagonal ring structure existing in NiMn-CPs and Ni-Mn-O intermediates disappears after high-temperature calcinations. The as-prepared $LiNi_{0.5}Mn_{1.5}O_4$ is in the shape of polyhedral blocks with a radical length of 1 ~ 3 μm. Furthermore, the polyhedral $LiNi_{0.5}Mn_{1.5}O_4$ blocks in Fig. 3f are observed to be composed of the nanoplate assemblies with approximate dimensions of 80 nm × 100 nm. In the detailed TEM images of the nanoplates as shown in Fig. 1g-i, a coating layer with a certain thickness can be vividly observed on the surface of the as-prepared "+8%", "+15%" and "+20%" materials. The thickness of the coating layer is 2 nm, 6 nm and 7 nm corresponding to the samples of "+8%", "+15%" and "+20%", respectively. The high-resolution TEM image for "+15%" sample as shown in Fig. 1j displays two legible neighboring lattice fringes with approximate values of 0.473 nm and 0.403 nm, which match the interspaces of (111) and (002) of the cubic spinel $LiNi_{0.5}Mn_{1.5}O_4$, respectively. Besides, the surface coating layer with a thickness of 6 nm can be also obviously observed from the HRTEM image. The SAED pattern as shown in Fig. 1k indicates the final product is $LiNi_{0.5}Mn_{1.5}O_4$ monocrystalline assigned to the $Fd\bar{3}m$ space group.

The X-ray diffraction (XRD) patterns of the as-prepared final products are shown in Fig. 2. All peaks in the XRD patterns can be indexed as the spinel $LiNi_{0.5}Mn_{1.5}O_4$ phase (JCPDS No. 80-2162) with typical intensive peaks, such as (111), (311) and (400). It is confirmed that the spinel $LiNi_{0.5}Mn_{1.5}O_4$ was successfully synthesized by using the NiMn-CPs as the precursors. It can be observed from Fig. 2 that the $Li_xNi_{1-x}O$ phase,[6, 38] a common concomitant impurity phase in $LiNi_{0.5}Mn_{1.5}O_4$ materialsis absent in the whole patterns. This phenomenon indicates that ptcda plays an important role via its strong coordination with the transition metal ions in preventing the formation of impurity phase in the $LiNi_{0.5}Mn_{1.5}O_4$ products. Furthermore, the lattice constants were calculated from the Rietveld refinement method, which are 8.1744 Å, 8.1757 Å and 8.1708 Å for the "+8%", "+15%" and "+20%" samples, respectively.

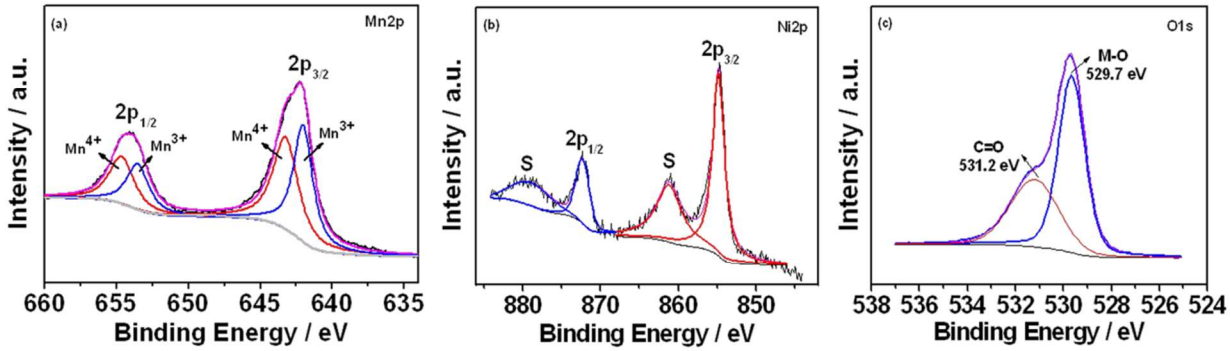

Fig. 3 X-ray photoelectron spectroscopy collected at (a) Mn2p, (b) Ni2p and (c) O1s regions of the "+15%" $LiNi_{0.5}Mn_{1.5}O_4$ sample.

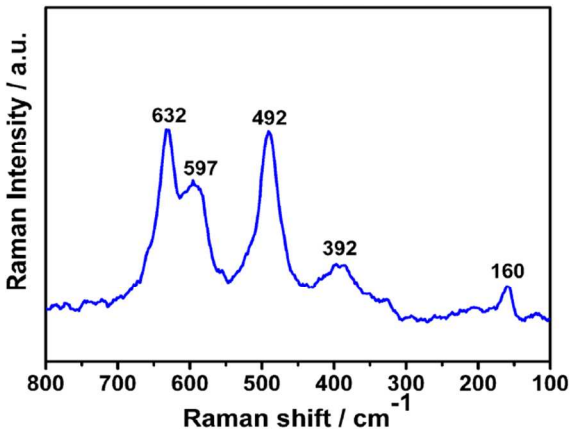

Fig. 4 Raman spectrum for the "+15%" sample.

By employing ICP tests, the chemical compositions of the three samples can be estimated as $Li_{1.010}Ni_{0.496}Mn_{1.504}O_4$, $Li_{1.063}Ni_{0.495}Mn_{1.505}O_4$, and $Li_{1.094}Ni_{0.498}Mn_{1.502}O_4$ corresponding to the "+8%", "+15%" and "+20%" sample, respectively. There is no linear relationship between the lattice constants and the Li content in the samples, which is disobedient to the Vegard's rule. Therefore, it is rational to assume that not all the lithium has been doped into the crystal structure of the spinel and a portion of lithium in excess could possibly participate in the formation of the Li-containing surface layer.

In order to get a better understanding of the surface chemical compositions, the "+15%" $LiNi_{0.5}Mn_{1.5}O_4$ was selected to be investigated by X-ray photoelectron spectra (XPS). The results are presented in Fig. 3a-c. The Mn2p spectrum includes two peaks which can be ascribed to the manganese 2p3/2 at 642.4 eV and 2p1/2 at 654.1 eV with a spin-energy separation of 11.7 eV. This result is in good agreement with the previous reports for $Mn2p_{3/2}$ and $Mn2p_{1/2}$ in Mn^{4+} components.[39, 40] According to MnO_2 and Mn_2O_3 spectral lines, both of the manganese $2p_{3/2}$ and $2p_{1/2}$ regions can be deconvoluted into two peaks. The peaks at 642.0 and 643.3 eV (as marked) of the $Mn2p_{3/2}$ spectrum in Fig. 3a are attributed to Mn^{3+} and Mn^{4+}, respectively, as well as those at 653.5 eV for Mn^{3+} and 654.6 eV for Mn^{4+} in the $Mn2p_{1/2}$ spectrum.[6, 41-43] Four features can be easily discerned in the Ni2p region in Fig. 3b. The main peak and its satellite for $Ni2p_{3/2}$ are at 854.7 eV and 861.2 eV, respectively, while those of $Ni2p_{1/2}$ are at 872.2 and 879.4 eV, respectively. The observed satellite peaks can be ascribed to the multiple splitting of the energy levels of nickel oxide NiO.[5, 42]

The O1s XPS spectrum as shown in Fig. 3c is mainly composed of two peaks - one is assigned to the oxygen in M-O (M refers to the metal ion) existing in the crystal lattice,[44, 45] and the other to the oxygen in carbonate species ($-CO_3^{2-}$).[45-48] The narrow peak at 529.8 eV is the characteristic of oxygen atoms in the crystalline network, while the broad peak with low intensity at 531.2 eV could be assigned to some carbonate species at the surface of the material.[45-47] Based on the results obtained with XRD and ICP, the observation of the carbonate species suggests the existence of Li_2CO_3. The amorphous surface layer of Li_2CO_3 may be possibly generated from the reaction of Li_2O (the decomposition product of lithium acetate) with CO_2 and moisture in the surrounding atmosphere at temperature below 900 °C during the cooling process.[49-51] It is expected that the surface layer of Li_2CO_3 could suppress the side reactions of the active cathode material $LiNi_{0.5}Mn_{1.5}O_4$ with the electrolyte by reducing the contact interface, thus favoring the cyclic stability.

Raman spectroscopy can be employed to distinguish between the disordered $Fd\bar{3}m$ and ordered $P4_332$ space groups of spinel structure.[5, 52, 53] Thus the Raman spectrum of the "+15%" $LiNi_{0.5}Mn_{1.5}O_4$ sample was measured and shown in Fig. 4. According to the previous reports, the strongest Raman peak in $LiNi_{0.5}Mn_{1.5}O_4$ is around 635 cm^{-1} and can be assigned to the symmetric Mn-O stretching mode of MnO_6 octahedra (A1g).[5, 23, 52, 53] The peaks around 402 and 491 cm^{-1} are associated with the Ni^{2+}-O stretching mode in the crystallite structure.[5, 23, 53] The splitting of $T2g^3$ band near 580 ~ 606 cm^{-1}, an obvious evidence of the ordered structure of $P4_332$ for the spinel,[53] is absent in the Raman spectra of the "+15%" $LiNi_{0.5}Mn_{1.5}O_4$ sample. In addition, the characteristic bands around 239, 218 and 161 cm^{-1} for $P4_332$ structure cannot be observed in the collected data either. Therefore, the peaks in Fig. 4 are the fingerprints of $Fd\bar{3}m$ phase in $LiNi_{0.5}Mn_{1.5}O_4$ rather than $P4_332$ phase, which is in consistence with the information obtained from SAED and XRD patterns. It is indicated that the F-type material with a portion of redox-active Mn^{3+} presents higher electronic conductivity which is benefit to improve the electrochemical properties of the material.

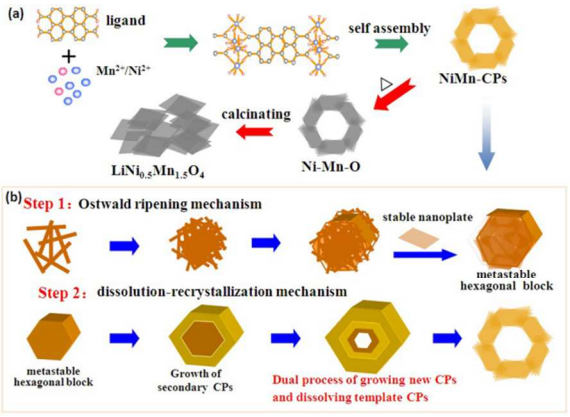

Fig. 5 Schematic illustrations of the morphology evolution during the synthesis process, particularly the proposed formation mechanism of nanoplate stacked $LiNi_{0.5}Mn_{1.5}O_4$ materials.

A possible mechanism for the formation of nanoflake-stacked $LiNi_{0.5}Mn_{1.5}O_4$ is illustrated in Fig. 5. Due to the strong coordination of ptcda with the transition metal ions, the yellow precipitation of NiMn-CPs is observed to be easily generated at room temperature as soon as ptcda solution was added into the mixed acetate solution of Ni and Mn. When in a hydrothermal atmosphere, the ptcda ligand with a rigid and planar molecule structure acts as a template to promote the formation of nanoplates and metastable hexagonal blocks by "layer-by-layer" assembly via the Ostwald ripening mechanism described as step 1 in Fig. 5b. Afterward, the metastable hexagonal NiMn-CPs blocks play two roles: one is served as the template to laterally overgrow the polymer, and the other one as the active center for the template dissolution. This process can be described as a "self-template directed mechanism" (dissolution-recrystallization mechanism, described as step 2 in Fig. 5b) proposed in the previous reports.[34, 54] The Ni-Mn-O materials with the same structure as that of the NiMn-CPs are obtained by removing the organic components using a thermal treatment. In the final calcination process, the hexagonal rings completely disappear, and the $LiNi_{0.5}Mn_{1.5}O_4$ nanomaterials with nanoplate morphology are synthesized, This novel nanoplate morphology can favor to improve the electrochemical properties especially the rate capability.

Fig. 6a displays the cyclic voltammetric curve obtained with the "+15%" $LiNi_{0.5}Mn_{1.5}O_4$ sample. The two couples of redox current peaks appearing in the potential range of 4.60 V ~ 4.79 V are attributed to the two-step oxidation/reduction of Ni^{2+}/Ni^{3+} and Ni^{3+}/Ni^{4+}, respectively.[2, 29] The small redox current peaks around 4.0 V are ascribed to the redox reaction of Mn^{3+}/Mn^{4+}.[3, 6, 29] The potential difference between the anodic and cathodic current peaks of Ni^{2+}/Ni^{3+} and Ni^{3+}/Ni^{4+} is 0.11 V and 0.14 V, respectively, indicating fast lithium extraction/insertion kinetics.

The galvanostatic charge and discharge profiles obtained with the half-cell using the $LiNi_{0.5}Mn_{1.5}O_4$ cathode are presented in Fig. 6b. In the charging process, all the $LiNi_{0.5}Mn_{1.5}O_4$ cathodes exhibited a short and not obvious plateau around 4.0 V which can be easily indentified in the discharge profiles, then followed by two long and distinct flat plateaus in the region of 4.60 ~ 4.80 V. The potential plateau at 4.0 V is corresponding to the oxidation of

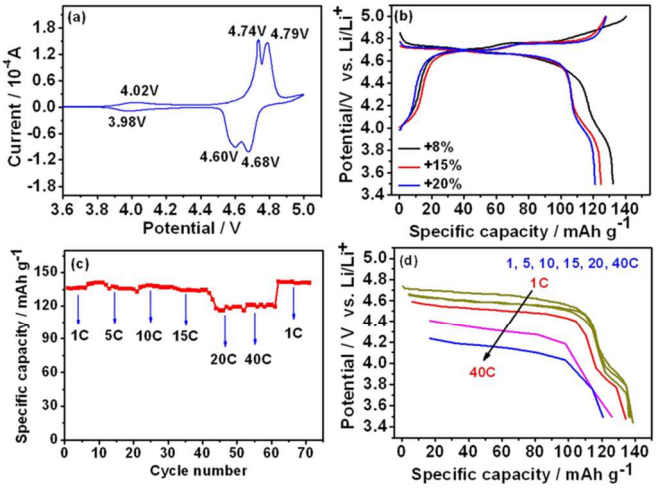

Fig. 6 (a) Cyclic voltammograms (CV) curve obtained with the "15%" sample, scanned at 0.05 mV s^{-1}; (b) Typical charge-discharge curves obtained with the "+8%", "+15%" and "+20%" samples of $LiNi_{0.5}Mn_{1.5}O_4$ at 1 C (147 mAh g^{-1}) between 3.5 and 5.0 V;. Rate capability (c) and discharge profiles (d) of the "+15%" sample tested at various discharge rates.

Mn^{3+} to Mn^{4+}, indicating that the obtained $LiNi_{0.5}Mn_{1.5}O_4$ is of $Fd\bar{3}m$ structure. This is in good agreement with the results obtained from XRD and Raman characterizations. Corresponding to the oxidation current peaks at 4.74 V and 4.79 V in the CV curve, the two upper plateaus around 4.70 V are attributed to the oxidation reactions of $Ni^{2+} \rightarrow Ni^{3+}$ and $Ni^{3+} \rightarrow Ni^{4+}$, which contribute to the major capacities. The "+8%", "+15%" and "+20%" $LiNi_{0.5}Mn_{1.5}O_4$ cathode materials delivered discharge specific capacity of 132.1 mAh g^{-1}, 124.7 mAh g^{-1} and 121.2 mAh g^{-1} respectively, which decreased with increasing the content of the inert Li_2CO_3 component.

Since high power density of the battery is highly demanding in PHEVs and EVs, the rate capability of the cathode material is especially important. To evaluate the high rate capability, the "+15%" sample was charged at 1 C rate and discharged at various rates as described in experimental section. As shown in Fig. 6c, the sample delivered a specific discharge capacity of 134.2 mAh g^{-1} at 15 C and 120.9 mAh g^{-1} even at 40 C, which is 95.2% and 85.8% of 140.9 mAh g^{-1} obtained at 1 C, respectively. Moreover, the average working voltage can still maintain at 4.39 V and 4.10 V at 15 C and 40 C respectively, as shown in Fig. 6d. Our results are superior to the previously reported values in which the specific capacities were less than 120 mAh g^{-1} and the average working voltages were in the range of 4.1 ~ 4.3 V when the discharging rate was 20 C[55-57], or the average working voltages was 3.90 V when the discharging rate was 40 C.[58] It is thus demonstrated that the "+15%" sample presents an outstanding rate performance that possibly benefits from the nanoplate-stack structure.

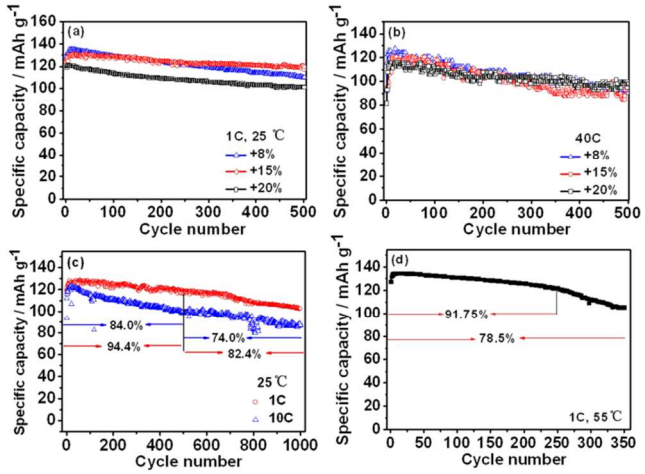

Fig. 7 Galvanostatic cycling test for the three samples at discharge rate of (a) 1 C and (b) 40 C at 25 ℃. The long-term cycling performance of the "+15%" sample at 25 ℃ (c) and 55 ℃ (d).

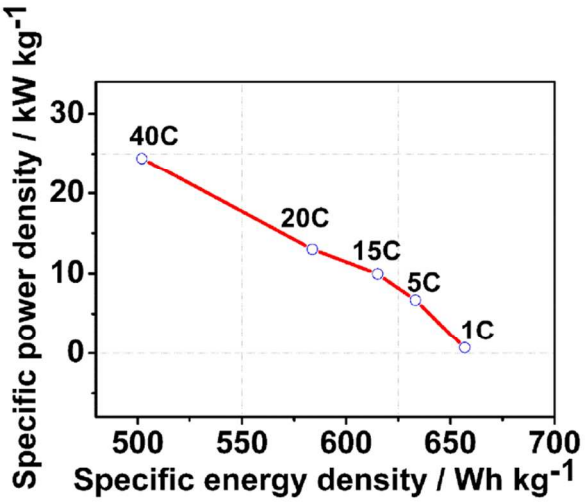

Fig. 8 Ragone plot (Specific power density vs. Specific energy density) for consequently,

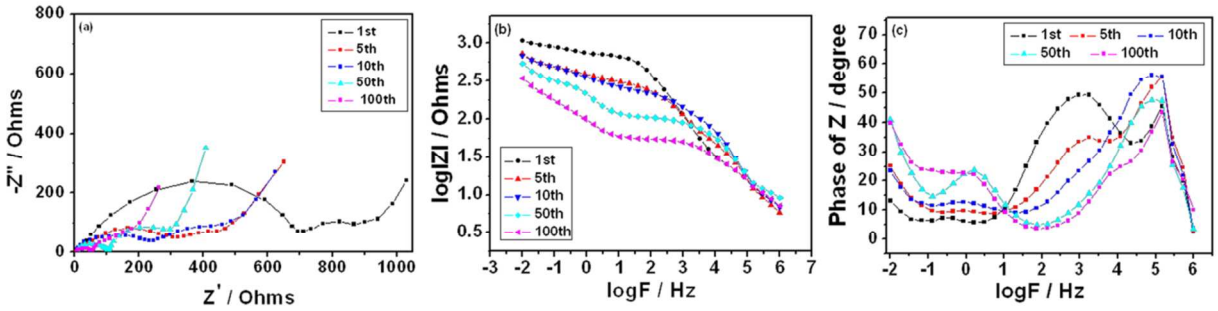

Fig. 9 (a) Nyquist plots and (b) the corresponding Bode magnitude and (c) phase plots measured using the half-cell with the "+15%" sample as cathode at fully discharged state, respectively.

The cycling performance of the as-prepared $LiNi_{0.5}Mn_{1.5}O_4$ material is presented in Fig. 7. At 25 ^oC, after several cycles of charge-discharge, the "+8%", "+15%" and "20%" samples deliver the largest specific discharge capacities of 134.0, 129.8 and 119.3 mAh g^{-1} at 1 C rate and retain 81.9%, 92.3% and 84.7% of the largest capacities after 500 charge-discharge cycles, respectively (as shown in Fig. 7a). Moreover, even at a higher discharge rate of 40 C, the specific discharge capacities of 122.5, 115.1 and 111.1 mAh g^{-1} and the capacity retentions of 74.8%, 85.1% and 88.3% after 500 cycles can be achieved for the "+8%", "+15%" and "20%" samples, respectively (as shown in Fig. 7b). In order to fully estimate the long-term cycling performance of the as-prepared $LiNi_{0.5}Mn_{1.5}O_4$ at 25 ^oC, the "+15%" sample was galvanostatically charged and discharged for 1000 cycles using discharge rate of 1 C and 10 C, respectively, and the results are shown in Fig. 7c. Activated upon cycling, the "+15%" sample can deliver 124.6 and 117.7 mAh g^{-1} at 1 C and 10 C, with the capacity retention of 82.4% and 74.0% for the 1000th cycle, respectively. The cycling properties of the $LiNi_{0.5}Mn_{1.5}O_4$ materials in this work can compare favorably with the values previously reported,[24, 30, 59, 60] in which the capacity retention was about 80% of the initial capacity after 500 cycles at 10 C rate,[59] or maintained less than 90% of the initial capacity after only 200 cycles at 20 C rate.[24, 30] Besides, a few literatures have reported the long-term cycling property extending over 500 cycles.[59-62] The $LiNi_{0.5}Mn_{1.5}O_4$ material prepared in this work, "+15%" sample with data derived from Figure 6c. exhibits superior electrochemical performance.

The cycling property of the "+15%" $LiNi_{0.5}Mn_{1.5}O_4$ at an elevated temperature of 55 ^oC was also investigated. The evolution of the specific capacity vs. cycles at 55 ^oC is presented in Fig. 7d. The material delivers more than 134.0 mAh g^{-1} with the capacity loss by cycle of 0.037% during 250 cycles at 55 ^oC. Although the stability deteriorated in the further cycling, the material still maintained capacity retention of 83.4% after 300 cycles. Its excellent cycling performance can be comparable to the data previously reported for the spinel analogues.[23, 56, 63-66] For instance, Rh-doped $LiNi_{0.5}Mn_{1.5}O_4$ was reported to maintain 83.6% of its initial capacity after 300 cycles under a 150 mA g^{-1} current at 55 ^oC.[56] $LiNi_{0.5}Mn_{1.5}O_4$ spinel prepared by sol–gel method had a reversible capacity of ~ 116 mAh g^{-1} and capacity retention of 89.2% after 200 cycles at 55 ^oC.[66]

Ragone plot for the "+15%" sample at different discharge rates is presented in Fig. 8. As increasing the discharging rate from 1 C to 40 C, the energy density of the material decreases from 657 Wh kg^{-1} to 501 Wh kg^{-1}. However, the power density of the material increases greatly from 0.685 kW kg^{-1} to 24.4 kW kg^{-1}. Thus the nanoplate-stacked $LiNi_{0.5}Mn_{1.5}O_4$ cathode materials exhibit high density of energy and power, which can be comparable with the performance reported in the previous reports.[57, 67, 68]

Fig. 9a-c shows the Nyquist plots and the corresponding Bode plots measured with the fully discharged half-cell using the "+15%" $LiNi_{0.5}Mn_{1.5}O_4$ as the cathode material. All the EIS measurements were carried out at room temperature. As can be observed from Fig. 9a that each of the impedance spectra

includes three parts: a semicircle in the high-frequency region reflects the resistance for Li^+ migration through the surface film and the capacitance of the film; another semicircle in the medium-to-low frequency region refers to charge-transfer resistance and the interfacial capacitance between the electrode and electrolyte; and a sloping line at very low frequencies is associated with Li^+ ion diffusion in the bulk material. It can be observed from Fig. 9a that the first semicircles in the high-frequency region obviously decrease in the diameter as the cycle number increase from 1 to 100. This suggests that the surface film has a dynamic optimization process and resistance for Li^+ migration becomes smaller. The charge-transfer resistance and interfacial capacitance also decrease, as indicated in the medium-to-low frequency region of the Bode magnitude plot (Fig. 9b). It can be concluded that the half-cell experience activations in the regions of surface film and the surface film/active mass interface. In the low-frequency region as shown in Fig. 9c, the phase peaks shift to a higher value of frequency as the cycle number increases, which indicates that the structure of $LiNi_{0.5}Mn_{1.5}O_4$ possibly changes, thus affecting the Li^+ insertion and extraction in the bulk material. During the charging-discharging process, the electrochemical impedance of the half-cell involves complicated issues, such as the relaxation and optimization of the SEI film and Li_2CO_3 coating layer, and the "Li-depleted" and "Li-rich" regions as well as the structural distortion generated in the bulk of $LiNi_{0.5}Mn_{1.5}O_4$. Therefore more intensive and systematic investigations will be performed in our future study.

4 Conclusions

The $LiNi_{0.5}Mn_{1.5}O_4$ nanoplates coated by a nano-scale Li_2CO_3 surface layer were prepared using a hydrothermal method to generate the bimetal-organic coordination-polymer (NiMn-CPs) as the precursor, then followed by a solid-state reaction with lithium acetate. The rigid and planar molecular structure of ptcda promotes the formation of nanoplate-stacked NiMn-CPs. After heat-treatment, the organic components in NiMn-CPs were removed to generate the bimetal oxides of Ni and Mn (Ni-Mn-O). Finally, $LiNi_{0.5}Mn_{1.5}O_4$ nanoplates were successfully synthesized by calcinating the Ni-Mn-O with the lithium salts. Additionally, a surface layer of Li_2CO_3 with nanometer thickness on the $LiNi_{0.5}Mn_{1.5}O_4$ particles was confirmed by TEM and XPS. It is found that the sample synthesized with +15% excess lithium salts exhibits the best electrochemical performance and cycling performance, especially at high temperature. The "+15%" sample shows excellent rate capability with a reversible capacity of 120.9 mAh g^{-1} at a discharge rate of 40 C and exhibits 128.2 mAh g^{-1} at 1 C rate with the capacity retention of 86.4% even over 1000 cycles at 25 °C. Even at 55 °C, the capacity loss by cycle is only 0.37‰ over 250 cycles. A synthetic strategy to synthesis insertion materials with nanoflake-stacked structure and in-situ Li_2CO_3 coating layer is introduced for lithium-ion batteries with high power and long lifetime, making their application in EVs and PHEVs feasible.

Notes and references

[a] *Advanced rechargeable battery Laboratory, Dalian Institute of Chemical Physics, Chinese Academy of Sciences, 457 Zhongshan Road, Dalian116023, China. Fax: +86-411-84379687; Tel: +86-411-84379687 E-mail: chenjian@dicp.ac.cn;*
[b] *Graduate School of the Chinese Academy of Sciences, Beijing 100049,China*

†Electronic Supplementary Information (ESI) available:

1. D. Liu, J. Hamel-Paquet, J. Trottier, F. Barray, V. Gariépy, P. Hovington, A. Guerfi, A. Mauger, C. M. Julien, J. B. Goodenough and K. Zaghib, *J.Power Sources*, 2012, **217**, 400-406.
2. J. H. Kim, C. S. Yoon, S. T. Myung, J. Prakash and Y. K. Sun, *Eletrochem. Solid-State Lett.*, 2004, **7**, A216-A220.
3. M.Kunduraci and G. G.Amatucci, *J. Electrochem. Soc.*, 2006, **153**, A1345-A1352.
4. J.-H. Kim, N. P. W. Pieczonka, Z. Li, Y. Wu, S. Harris and B. R. Powell, *Electrochim. Acta*, 2013, **90**, 556-562.
5. J. S. Park, K. C. Roh, J.-W. Lee, K. Song, Y.-I. Kim and Y.-M. Kang, *J. Power Sources*, 2013, **230**, 138-142.
6. C. J. Jafta, M. K. Mathe, N. Manyala, W. D. Roos and K. I. Ozoemena, *Appl. Mater. Interfaces*, 2013, **5**, 7592-7598.
7. B. Arman, Q.M. Zhong, M. J. Zhang, Y. Gao and J. R. Dahn, *J. Electrochem. Soc.*, 1997, **144**, 205-213.
8. J. F. A.-S. M. Kunduraci, and G. G. Amatucci, *Chem. Mater.*, 2006, **18**, 3585-3592.
9. X. W. Wu, X. H. Li, Z. X. Wang, H. J. Guo, J. X. Wang and P.Yue, *J. Solid State Electr.*, 2012, **17**, 1029-1038.
10. J. L. Demeaux, D. Lemordant, M. Caillon-Caravanier, H. Galiano and B. Claude-Montigny, *Electrochim. Acta*, 2013, **89**, 163-172.
11. N. P. W. Pieczonka, Z. Y. Liu, P. Lu, K. L.Olson, J. Moote, B. P. Powell and J.-H. Kim, *J. Phys. Chem. C*, 2013, **117**, 15947-15957.
12. J. M. Zheng, J. Xiao, X. Q. Yu, L.Kovarik, M. Gu, F. Omenya, X. L. Chen, X. Q.Yang, J. Liu, G. L. Graff, M. S.Whittingham and J. G. Zhang, *Phys. Chem. Chem. Phys.*, 2012, **14**, 13515-13521.
13. Y. Idemoto, H. Narai and N. Koura, *J. Power Sources*, 2003, **119-121**, 125-129.
14. G. Q. Liu, L. Wen, X. Wang and B. Y. Ma, *J. Alloys Compd.*, 2011, **509**, 9377-9381.
15. J. Liu and A. Manthiram, *J. Phys. Chem. C*, 2009, 15073-15079.
16. H. Wang, T. A. Tan, P. Yang, M. O. Lai and L. Lu, *J. Phys. Chem.C*, 2011, **115**, 6102-6110.
17. C. Locati, U. Lafont, L. Simonin, F. Ooms and E. M. Kelder, *J. Power Sources*, 2007, **174**, 847-851.
18. T. Noguchi, I. Yamazaki, T. Numata and M. Shirakata, *J. Power Sources*, 2007, **174**, 359-365.
19. M. Aklalouch, J. M. Amarilla, R. M. Rojas, I. Saadoune and J. M. Rojo, *J. Power Sources*, 2008, **185**, 501-511.
20. J. Liu and A. Manthiram, *J. Electrochem. Soc.*, 2009, **156**, A66-A72.
21. M.-L.-P. Le, P. Strobel, F. Alloin and T. Pagnier, *Electrochim. Acta*, 2010, **56**, 592-599.
22. O. Sha, Z. Tang, S. Wang, W. Yuan, Z. Qiao, Q. Xu and L. Ma, *Electrochim. Acta*, 2012, **77**, 250-255.
23. G. B. Zhong, Y. Y. Wang, Y. Q. Yu and C. H. Chen, *J. Power Sources*, 2012, **205**, 385-393.
24. O. Sha, Z. Qiao, S. L. Wang, Z. Y. Tang, H. Wang, X. H. Zhang and Q. Xu, *Mater. Res. Bull.*, 2013, **48**, 1606-1611.
25. M. Aklalouch, R. M. Rojas, J. M. Rojo, I. Saadoune and J. M. Amarilla, *Electrochim. Acta*, 2009, **54**, 7542-7550.
26. D. Liu, J. Trottier, P. Charest, J. Fréchette, A. Guerfi, A. Mauger, C. M. Julien and K. Zaghib, *J. Power Sources*, 2012, **204**, 127-132.
27. Z. Qiao, O. Sha, Z. Y. Tang, J. Yan, S. L. Wang, H. B. Liu, Q. Xu and Y. J. Su, *Mater. Lett.*, 2012, **87**, 176-179.
28. G. Y. Zhao, Y. B. Lin, T. Zhou, Y. Lin, Y. D. Huang and Z. G. Huang, *J. Power Sources*, 2012, **215**, 63-68.
29. J. Chong, S. D. Xun, X. Y. Song, G. Liu and V. S. Battaglia, *Nano Energy*, 2013, **2**, 283-293.
30. O. Sha, S. Wang, Z. Qiao, W. Yuan, Z. Tang, Q. Xu and Y. Su, *Mater. Lett.*, 2012, **89**, 251-253.
31. D. I. Choi, H. Lee, D. J. Lee, K. W. Nam, J. S. Kim, R. A. Huggins,

J. K. Park and J. W. Choi, *J Mater Chem A*, 2013, **1**, 5320-5325.
32. X. Zhang, F. Cheng, J. Yang and J. Chen, *Nano lett.*, 2013, **13**, 2822-2825.
33. J. Zhao, M. R. Li, J. L. Sun, L. F. Liu, P. P. Su, Q. H. Yang and C. Li, *Chem. Eur. J.*, 2012, **18**, 3163-3168.
34. J. Zhao, P. P. Su, Y. P. Zhao, M. R. Li, Y. Yang, Q. H. Yang and C. Li, *J. Mater. Chem.*, 2012, **22**, 8470-8475.
35. J. Zhao, F. Q. Wang, P. P. Su, M. R. Li, J. Chen, Q. H. Yang and C. Li, *J. Mater. Chem.*, 2012, **22**, 13328-13333.
36. W.S. Kim, K.-I. Chung, J. H. Cho, D. W. Park, C. Y. Kim, Y. K. Choi, *J. Ind. Eng. Chem.*, 2003, **9**, 699-703.
37. K.-I. Chung, J.-D. Lee, E.-J. Kim, W.-S. Kim, J.-H. Cho and Y.-K. Choi, *Microchem. J.*, 2003, **75**, 71-77.
38. X. Zhang, F. Cheng, K. Zhang, Y. Liang, S. Yang, J. Liang and J. Chen, *RSC Adv.*, 2012, **2**, 5669-5675.
39. N. Yabuuchi, K. Yoshii, S. T. Myung, I. Nakai and S. Komaba, *J. Am. Chem. Soc.*, 2011, **133**, 4404-4419.
40. S. J. R. Prabakar, S. C. Han, S. P. Singh, D. K. Lee, K.-S. Sohn and M. Pyo, *J. Power Sources*, 2012, **209**, 57-64.
41. J.-Y. Shi, C.-W. Yi, L. H. Liang and K. Kim, *B. Kor. Chem. Soc.*, 2010, **31**, 309-314.
42. X. G. Hao, M. H. Austin. and B. M. Bartlett. *Dalton Trans.*, 2012, 8067-8076.
43. X. F. Sun, Y. L. Xu, M. R. Jia, P. Ding, Y. H. Liu and K. Chen, *J. Mater. Chem. A*, 2013, **1**, 2501-2507.
44. L. Dahe´ron, H. Martinez. R. Dedryvere, I. Baraille, M. Me´ne´trier, C. Denage, C. Delmas and D. Gonbeau, *J. Phys. Chem. C* 2009, **113**, 5843-5852.
45. M. Q. Xu, D. S. Lu, A. Garsuch and B. L. Lucht, *J. Electrochem. Soc.*, 2012, **159**, A2130-A2134.
46. Y. K. Fan, J. M. Wang, Z. Tang, W. C. He and J. Q. Zhang, *Electrochim. Acta*, 2007, **52**, 3870-3875.
47. S. H. Wu and A. Huang, *J. Electrochem. Soc.*, 2013, **160**, A684-A689.
48. M. Herstedt, A. M. Andersson, H. Rensmo, H. Siegbahn and K. Edström, *Electrochim. Acta*, 2004, **49**, 4939-4947.
49. R. K. K. Matsumoto , K. Takeya, A. Yamanaka *J. Power Sources*, 1999, 558-561.
50. G. R. V. Zhuang, G. Y. Chen, J. Shim, X. Y. Song, P. N. Ross and T. J. Richardson, *J. Power Sources*, 2004, **134**, 293-297.
51. H. Konishi, K. Suzuki, S. Taminato, K. Kim, S. Kim, J. Lim, M. Hirayama and R. Kanno, *J. Power Sources*, 2014, **246**, 365-370.
52. N. Amdouni, K. Zaghib, F. Gendron, A. Mauger and C. M. Julien, *Ionics*, 2006, **12**, 117-126.
53. S. H. Oh, K. Y. Chung, S. H. Jeon, C. S. Kim, W. I. Cho and B. W. Cho, *J. Alloys Compd.*, 2009, **469**, 244-250.
54. S. Jung, W. Cho, H. J. Lee and M. Oh, *Angew. Chem. Int. Ed. Engl.*, 2009, **48**, 1459-1462.
55. Z. X. Chen, S. Qiu, Y. L. Cao, X. P. Ai, K. Xie, X. B. Hong and H. X. Yang, *J. Mater. Chem.*, 2012, **22**, 17768-17772.
56. P. Wu, X. L. Zeng, C. Zhou, G. F. Gu and D. G. Tong, *Mater. Chem. Phys.*, 2013, **138**, 716-723.
57. H. B. Lin, Y. M. Zhang, J. N. Hu, Y. T. Wang, L. D. Xing, M. Q. Xu, X. P. Li and W. S. Li, *J. Power Sources*, 2014, **257**, 37-44.
58. X. H. Ma, B. Kang and G. Ceder, *J.Electrochem. Soc.*, 2010, **157**, A925-A931.
59. Y. X. Qian, Y. F. Deng, Z. C. Shi, Y. B. Zhou, Q. C. Zhuang and G. H. Chen, *J. Electrochem. Soc.*, 2013, **27**, 92-95.
60. S. H. Choi, Y. J. Hong and Y. C. Kang, *Nanoscale*, 2013, **5**, 7867-7871.
61. X. Fang, M. Ge, J. Rong and C. Zhou, *J. Mater. Chem. A*, 2013, **1**, 4083.
62. Y. Xue, Z. Wang, F. Yu, Y. Zhang and G. Yin, *J. Mater. Chem. A*, 2014, **2**, 4185-4191
63. S. Patoux, L. Sannier, H. Lignier, Y. Reynier, C. Bourbon, S. Jouanneau, F. Le Cras and S. Martinet, *Electrochim. Acta*, 2008, **53**, 4137-4145.
64. K. M. Shaju and P. G. Bruce, *Dalton Trans.* , 2008, 5471-5475.
65. G. B. Zhong, Y. Y. Wang, X. J. Zhao, Q. S. Wang, Y. Yu and C. H. Chen, *J. Power Sources*, 2012, **216**, 368-375.
66. B. Li, L. Xing, M. Xu, H. Lin and W. Li, *Electrochem. Commun.*, 2013, **34**, 48-51.
67. M. Aklalouch, J. M. Amarilla, R. M. Rojas, I. Saadoune and J. M. Rojo, *Electrochem. Commun.*, 2010, **12**, 548-552.
68. H.-W. Lee, P. Muralidharan, C. M. Mari, R. Ruffo and D. K. Kim, *J. Power Sources*, 2011, **196**, 10712-10716.